Facile Ion Diffusion and High Electrical Conductivity Enable High-Energy and High-Power Sodium-Ion Batteries from a Layered Metal-Free Cathode

Tianyang Chen[1,3], Jiande Wang[1,3], Bowen Tan[1], Kimberly J. Zhang[1], Harish Banda[1], Yugang Zhang[2], Dong-Ha Kim[1], Mircea Dincă[1,4]*

[1]Department of Chemistry, Massachusetts Institute of Technology, Cambridge, MA 02139, United States

[2]Center for Functional Nanomaterials (CFN), Brookhaven National Laboratory, Upton, NY 11973, United States

[3]These authors contributed equally to this work

[4]Lead contact

*Correspondence: mdinca@mit.edu

Summary:

Sodium-ion batteries (SIB) attract considerable attention, but their practical implementation continues to suffer in large part from the limited energy density of current SIB cathode materials. In principle, redox-active organic materials can tackle this challenge because of their high theoretical energy densities. However, electrode-level energy densities of organic electrodes are compromised due to their poor electron/ion transport and severe dissolution. Here, we report the use of a low-bandgap, conductive, and highly insoluble layered metal-free cathode material for SIBs. It has a high theoretical capacity and enables a practical-level active material content, achieving an electrode-level energy density of 606 Wh $kg^{-1}_{electrode}$ and long cycle life. It allows for facile two-dimensional Na^+-ion diffusion, which enables high intrinsic rate capability. In-situ growth of the active cathode material with carbon nanotubes, which improves charge transport and charge transfer kinetics, further enhances the power performance. Altogether, these allow the construction of full SIB cells built from an affordable, sustainable organic small molecule, which provide a cathode energy density of 472 Wh $kg^{-1}_{electrode}$ when charging/discharging in 90 seconds, a top specific power of 31.6 kW $kg^{-1}_{electrode}$.

Context & scale

Owing to sodium's natural abundance, sodium-ion batteries (SIBs) have attracted tremendous attention as a promising alternative technology to lithium-ion batteries (LIBs), especially for stationary energy storage and moderate-range electric vehicles. The practical implementation of SIBs, however, continues to suffer in large part from the limited energy density of current inorganic cathode materials. Here, we report the use of a low-bandgap, electrically conductive, and insoluble layered metal-free cathode material for SIBs. This redox-active organic material achieves an electrode-level energy density that outperforms most existing cathode materials, and exhibits exceptional cycle life. It allows for facile two-dimensional Na^+-ion diffusion, which enables high intrinsic rate capability. In-situ growth of the active cathode material with carbon nanotubes, which improves charge transport and charge transfer kinetics, further enhances the power performance. Altogether, these allow the construction of sustainable, high-energy SIBs that can charge/discharge within a minute.

Main text:

Owing to sodium's widespread availability, sodium-ion batteries (SIBs) have attracted tremendous attention as a promising complementary technology to lithium-ion batteries (LIBs)[1], especially for stationary energy storage such as (micro)grids, data centers, and commercial-scale renewable energy systems. Cathode materials are pivotal to determining the performance of SIBs. Significant progress has been made with SIBs using various cathode materials, including layered transition metal oxides[2], Prussian blue analogues[3], and polyanionic compounds[4]. However, achieving both high energy density and high power density at the electrode level remains a major challenge.[5] While the former requires high specific capacity and high voltage, the latter demands facile ion and electron transport.

To overcome this challenge, redox-active organic electrode materials (OEMs), typically composed of earth-abundant elements like C, H, N, O, and S, have recently emerged as a promising solution, providing substantial opportunities due to their high theoretical specific capacity (e.g., > 350 mAh g^{-1}) and moderate redox potential (1.5 – 3 V vs. Na^+/Na).[6-7] These properties lead to a superior material-level energy density when compared to conventional inorganic cathode materials. However, at least 20 wt.% conductive carbon is generally required to turn these pure cathode materials into functional electrode compositions because traditional OEMs show inherently low electrical conductivity, often below 10^{-7} S m^{-1}. Cycling OEM-based SIBs at high rates also requires fast Na^+ transport, which in turn imposes new additive requirements: larger amounts of conductive carbon (> 40 wt.%) or 20-30 wt.% advanced carbon materials such as graphene and carbon nanotubes (CNTs) (Figure S1). This high additive requirement severely impairs the electrode-level energy density. On the one hand, employing low-energy gap OEMs with higher electrical conductivity would alleviate part of the carbon additive requirement. With respect to ionic transport, there is not a clear correlation between structural/compositional features and Na-ion diffusion, but it has been observed that crystalline networks that allow facile two-dimensional (2D) diffusion pathways, such as *T*-Nb_2O_5,[8] enable rapid intercalation of metal ions.

Clearly, employing a crystalline OEM that is electrically conductive and has an ordered 2D structure that could allow for fast Na-ion intercalation may be expected to reduce the need for carbon additives. However, a third problem arises with traditional OEMs: many materials in this class do not cycle well because they ultimately dissolve in the electrolyte. To prevent this, various additives are again employed. Alternative solutions that immobilize the active organic redox unit: polymerization[9-10], framework construction[11], and salinization[12-13] add significant "dead mass" that inevitably reduces the electrode-level energy and power densities (Figure S1). To this end, an ideal solution would be to a redox-active OEM that is intrinsically insoluble.

Here, we report the performance of a layered organic solid, TAQ (Figure 1a), as cathode material in SIBs. TAQ displays high energy and power density at the electrode level. TAQ comprises strongly hydrogen-bonded molecular 2D layers that address all previous challenges with OEMs in SIBs: the layered structure leads to narrow electronic bandgap with high electrical conductivity[14-15], it allows rapid intercalation and diffusion of Na^+ in-between layers, and the 2D hydrogen bonding lattice essentially eliminates solubility. TAQ-based cathodes exhibit a reversible specific capacity that nears the theoretical value of 355 mAh g^{-1} (Figure 1b), alongside fast charging/discharge capability, and long lifetime enabled by electrolyte optimization. Importantly, TAQ-based cathodes achieve a record high electrode-level energy density of 606 Wh $kg^{-1}_{electrode}$. *In-operando* studies reveal small reversible crystal-structural changes of TAQ during cycling, confirming the structural integrity of TAQ due to robust intermolecular interactions. Furthermore, electrode composite-level engineering through hydrogen-bonding assisted growth of

TAQ crystals with carboxyl functionalized single-walled carbon nanotubes (cSWCNTs) produces composites comprising TAQ crystals mixed with as little as ~2 wt.% cSWCNTs. Such composites exhibit significantly improved electrical conductivity due to close contact between TAQ crystallites and cSWCNTs. The TAQ-CNT composite electrodes exhibit ultrahigh rate capability, delivering 150 mAh g^{-1} at 20 A g^{-1} with an electrode-level power density of 31.6 kW $kg^{-1}_{electrode}$.

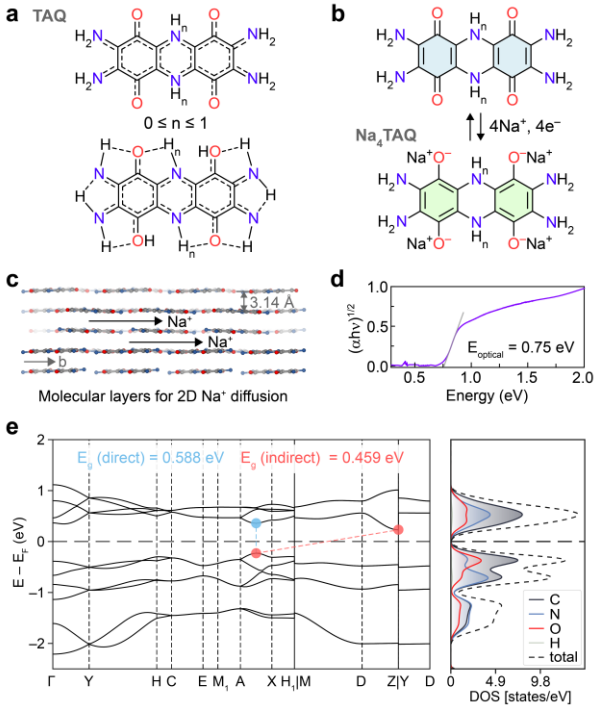

Figure 1. Designs and characterizations of TAQ. a, Molecular structure of TAQ, and its delocalized representation including hydrogen bonding. **b,** Na^+ storage chemistry of TAQ. **c,** The layered structure of TAQ with an interlayer distance of 3.14 Å. These molecular layers provide 2D diffusion pathways for Na^+. **d,** Diffuse reflectance UV-Vis-NIR spectrum of TAQ plotted in the Tauc coordinates, revealing an optical bandgap of 0.75 eV. **e,** Band structure and projected density of states of TAQ, revealing a direct electronic bandgap of 0.588 eV and an indirect electronic bandgap of 0.459 eV.

Characterizations of TAQ

As previously reported,[14-15] TAQ is isolated as micro-crystals wherein molecular TAQ units are held by pervasive hydrogen bonding into closely π–stacked 2D molecular layers (Figure 1c, Figure S2-S6). Previously described electron diffraction analysis identified only non-hydrogen atoms in the crystal structure; whereas the central C–N bond lengths (~1.41 Å) point to a dihydropyrazine formulation for the central ring, an oxidized ring (i.e. pyrazine) has also been proposed previously.[16] As such, TAQ is best described as any composition within the continuum $C_{12}H_{10-n}N_6O_4$ (n = 0 – 2) depending on whether the central pyrazine ring is oxidized or not. Importantly, because the hydrogen atoms do not participate in the Faradaic processes responsible for charge storage, the exact composition of TAQ within this compositional continuum bears no consequence on its electrochemical performance in a charge storage device, including batteries.

Due to significant intramolecular and intermolecular π–π interactions and hydrogen bonding, TAQ exhibits continuous electronic absorption from ultraviolet (UV) region to 1600 nm in its

ultraviolet–visible–near-infrared (UV-Vis-NIR) spectrum (Figure S7), resulting in an indirect optical bandgap of 0.75 eV (Figure 1d). This gap is smaller than those of most organic semiconductors. The semiconducting nature of TAQ is further demonstrated by band structure calculations with projected density of states (pDOS), which show that TAQ has an indirect electronic bandgap of 0.459 eV (Figure 1e). Furthermore, the curvature of the bands along the high symmetry points in the reciprocal space suggests that the electrons have reasonable mobility. The pDOS diagram also reveals that carbon atoms contribute significantly to the valence band, indicating significant π-π stacking interactions. Therefore, TAQ possesses promising charge transport properties, which is in stark contrast to typical OEMs with large bandgaps. Indeed, with a high electrical conductivity of 2.56×10^{-2} mS cm^{-1} (Figure S8), TAQ compares favorably to all other cathode materials for SIBs.[17-18]

Importantly, TAQ is insoluble in common organic solvents due to its robust intermolecular interactions, such that TAQ electrodes exhibit no dissolution after soaking in SIB electrolytes for at least eight months (Figure S9). TAQ can accommodate up to four Na^+ ions per formula unit, through the reduction of carbonyl groups (Figure 1b), offering a theoretical specific capacity of 355 mAh g^{-1}. The insolubility and desirable electron and ion transport features of TAQ enable the fabrication of TAQ-CB*x* cathodes (CB: carbon black; *x* indicates the weight percentage of CB), which consist as high as 90 wt.% TAQ and as low as 5 wt.% CB (Figure 2a inset).

Intrinsic facile Na^+ diffusion in TAQ enables high rate capability

Na-ion half cells consisting of a TAQ-CB5 cathode, a metallic Na anode, and an ether-based electrolyte (1 M $NaPF_6$ in 1,2-dimethoxyethane (DME)/diethylene glycol dimethyl ether (Diglyme) (1:1))[19-21] were tested between 1.1 V and 3.1 V (all potentials are referenced to the Na^+/Na couple unless otherwise noted), a potential window optimized for practical use.[16] The initial discharge/charge cycle of a half cell measured under a current density of 25 mA g^{-1} exhibited a voltage profile (Figure 2a) with two discharge plateaus centered around 2.15 V and 1.5 V, which reveal roughly equal capacity, suggesting two $2e^-$ reduction processes per TAQ molecule. Cyclic voltammograms (CV) and dQ/dV curves (Figure S10, S11) both reveal three peaks at 1.7 V, 2.4 V, and 2.5 V during the charging process, corresponding to three plateaus in the charging voltage profile. The first plateau corresponds to a $2e^-$ oxidation, whereas the latter two correspond to two single-electron oxidations. The cell delivers a reversible discharge capacity of 325 mAh g^{-1} with an average discharge voltage of 2 V and a high initial coulombic efficiency (ICE) of 97.8%. Notably, although a TAQ-CB20 cathode (with 75 wt.% TAQ) delivers a higher active-material-level capacity of 337 mAh g^{-1} (Figure S12), the corresponding electrode-level capacity (i.e., based on the total mass of active material, CB, and binder), 253 mAh $g^{-1}_{electrode}$, is much lower than that of the TAQ-CB5 (with 90 wt.% TAQ) cathode, 286 mAh $g^{-1}_{electrode}$. Moreover, the TAQ-CB5 electrode exhibits average reversible discharge capacities of 298 mAh g^{-1} and 214 mAh g^{-1} at higher current densities of 100 mA g^{-1} and 1000 mA g^{-1}, respectively (Figure 2b). The capacity restores to 296 mAh g^{-1} when the current density changed from 2 A g^{-1} back to 100 mA g^{-1}, demonstrating the high rate capability and stability of TAQ-CB5 cathodes.

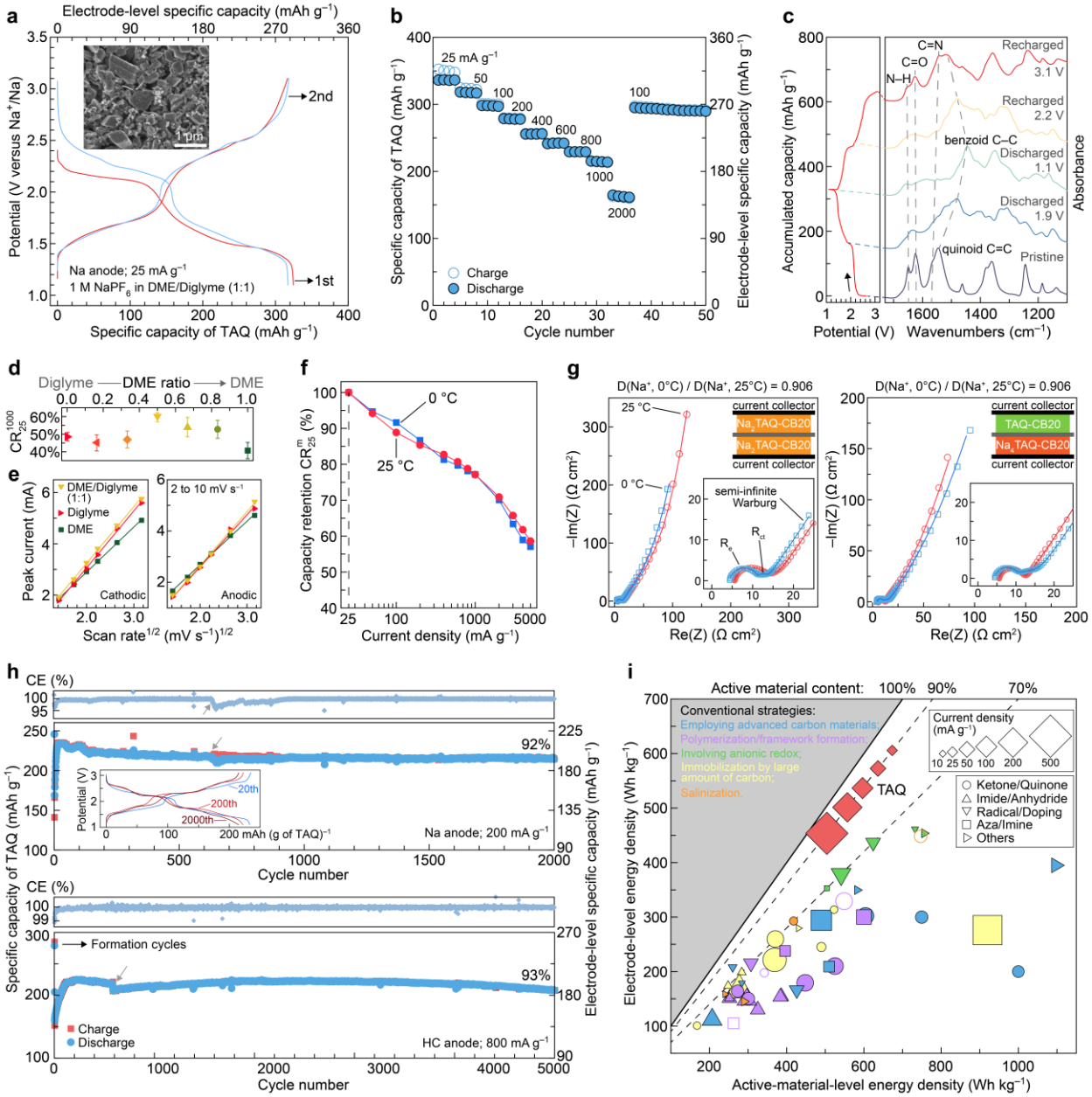

Figure 2. Battery performance of TAQ-CB cathodes. a, Galvanostatic charge-discharge voltage profiles of a TAQ-CB5||Na cell using 1 M $NaPF_6$ in DME/Diglyme (1:1) as the electrolyte. The first discharge plateau shifts up by approximately 0.1 V in the second cycle (blue trace), whereas the second discharge plateau stays roughly at the same voltage. Inset shows an SEM image of a TAQ-CB5 electrode. **b,** Rate capability study of a TAQ-CB5||HC (presodiated hard carbon) cell. **c,** *Ex-situ* DRIFT spectra of TAQ-CB5 cathodes at different states of charge and discharge. The C=O, C=N, quinoid C=C, and benzene C–C bands are located at 1624 cm^{-1}, 1568 cm^{-1}, 1546 cm^{-1}, and 1447 cm^{-1}, respectively. **d,** Rate capability comparisons of TAQ-CB5||Na cells using electrolytes with different ratios between DME and Diglyme. CR_{25}^{1000} results are average values based on 4~5 half cells for each ratio. **e,** The relationship between peak currents and scan rate plotted according to the Randles–Sevcik equation from CV measurements of half cells in DME, Diglyme, or DME/Diglyme (1:1) electrolytes. Solid lines represent the best linear fit. **f,** Capacity retention CR_{25}^{m} ($25 \leq m \leq 5000$) of TAQ-CB20||Na cells at 25 °C (red) and 0 °C (blue). The use of

20 wt.% CB ensures a good electron conduction in the electrode. **g,** Nyquist plots of TAQ-CB20 symmetric cells at 25 °C (red) and 0 °C (blue) with two different states of charge: Na_2TAQ-CB20||Na_2TAQ-CB20 (left), and TAQ-CB20||Na_4TAQ-CB20 (right). Solid lines represent the best fit. **h,** Cycling studies of a TAQ-CB5||Na cell at 200 mA g^{-1} (top), and a TAQ-CB5||HC cell at 800 mA g^{-1} (bottom). Insets show the evolution of voltage profiles during cycling. Gray arrows indicate disturbance of cycling studies due to unexpected power shutoff. **i,** Electrode-level energy density of state-of-the-art organic cathodes and the TAQ-CB cathode versus their energy density at the active-material level. The sizes of scatters represent current densities, and the colors of scatters correspond to common strategies to solve dissolution and insulation problems of OEMs. Hollow scatters represent organic electrodes whose average discharge voltage is less than or equal to 1.5 V, which is not ideal for cathodes.

Ex-situ diffuse-reflectance infrared Fourier Transform (DRIFT) spectra of TAQ-CB5 electrodes at different states of discharge and charge during the initial cycle confirm that both C=O and C=N are redox centers, as their stretching bands gradually disappear during discharging and recover upon charging (Figure 2c, Figure S13). This process is accompanied by the interconversion between the quinoid and the benzenoid structure, as evidenced by the shifting between the quinoid C=C stretching band and the benzene C–C stretching band. This spectroscopic evolution matches well with the redox mechanism of quinone-based compounds.[22-23]

Examination of TAQ-CB5 half-cells made with DME/diglyme electrolytes of varying composition provided insight into the intrinsic diffusion kinetics of Na^+ in TAQ (Figure S14). The capacity retentions at 1000 mA g^{-1} relative to 25 mA g^{-1} (denoted as CR_{25}^{1000}, where CR_n^m is defined as the capacity retention at *m* mA g^{-1} relative to *n* mA g^{-1}) in various electrolytes (Figure 2d) exhibit a volcano-like relationship with respect to the DME/diglyme ratio, with the DME/diglyme ratio of 1:1 leading to a peak CR_{25}^{1000} of 60%. Notably, such rate capability is normally achieved only when large amounts of carbon additives or surface carbon coatings are employed.[24-26] Further investigation of the electrolyte dependence using the Galvanostatic Intermittent Titration Technique (GITT) revealed apparent Na^+ diffusion coefficients (D_{Na^+}) in TAQ of approximately 10^{-10} cm^2 s^{-1} irrespective of the electrolyte composition when cycling at a low rate (25 mA g^{-1}) (Figure S15). This agrees with the nearly identical specific capacities obtained in these electrolytes at 25 mA g^{-1} (Figure S16). Interestingly, studies of the charge storage and ion transport under dynamic conditions using electrochemical impedance spectroscopy (EIS) reveal that TAQ-CB5||Na cells in DME and DME/Diglyme (1:1) electrolytes exhibit very similar charge transfer resistances (R_{ct}), which depend considerably on Na^+ intercalation kinetics (Figure S17 and Note S1). These values are significantly lower than those observed in the Diglyme electrolyte, suggesting that DME enhances the charge storage kinetics of TAQ. Surprisingly, *ex-situ* SEM images reveal severe exfoliation and pulverization of TAQ crystallites for cycled TAQ-CB5 electrodes in diglyme electrolyte, whereas neither DME nor DME/diglyme (1:1) electrolytes cause morphological alteration in TAQ-CB5 electrodes (Figure S18-S20). Even though diglyme thus seems detrimental to the integrity of TQ-CB, it is known as a good electrolyte for Na and hard carbon anodes.[27] As such, we opted for a 1 M $NaPF_6$ in DME/diglyme (1:1) as the optimized electrolyte that would balance the cathode and anode performance for TAQ-based SIBs.

To interrogate the mechanism giving rise to the high rate performance of TAQ, we carried out electrochemical kinetic studies through analyzing the currents from CV profiles of TAQ-CB5||Na cells using the power law relationship ($i = av^b$). We found that both cathodic and anodic peak currents are surface-controlled between scan rates of 0.1 mV s^{-1} and 2 mV s^{-1} (Figure S21 and

Table S1), suggesting that the charge storage behaves as a quasi-2D process and is controlled by the surface of TAQ 2D layers at relatively low rates.[8] Figure 2e shows the correlations between the cathodic or anodic peak currents and square root of scan rates between 2 mV s^{-1} and 10 mV s^{-1}, which fit well to a linear relationship for diffusion-controlled processes. Applying the Randles-Sevcik equation[28] yields estimated D_{Na^+} values of 8.5×10^{-9} cm^2 s^{-1} and 7.6×10^{-9} cm^2 s^{-1} for Na^+ intercalation and deintercalation, respectively, at moderate to high rates in the DME/Diglyme (1:1) electrolyte, which are higher than both DME and Diglyme electrolytes (Table S2). These values rank among the highest for all cathode materials for SIBs,[29] indicating facile Na^+ diffusion within the TAQ due to 2D diffusion pathways. More importantly, TAQ-CB20||Na cells exhibit very similar rate performance at 0 °C and 25 °C with high CR_{25}^{1000} values around 77% (Figure 2f, S22), implying almost temperature-independent rapid Na^+ diffusion. We further conducted EIS studies of symmetric cells[30-32] at two different states of charge, namely Na_2TAQ-CB20||Na_2TAQ-CB20 and TAQ-CB20||Na_4TAQ-CB20, under 0 °C and 25 °C to reveal solely the Na^+ diffusion kinetics in TAQ (see experimental procedures and Note S1). The ratios of D_{Na^+} (0 °C) over D_{Na^+} (25 °C) for the two states, calculated from the Warburg coefficients for semi-infinite diffusion within the bulk of TAQ particles, are both 90.6% (Figure 2g), suggesting a notably low Na^+ diffusion energy barrier. These results demonstrate that the facile 2D diffusion of Na^+ accounts for the intrinsic superior rate performance of TAQ-CB cathodes. The higher CR_{25}^{1000} for TAQ-CB20 cathodes than that for TAQ-CB5 cathodes also indicates that despite of the high electrical conductivity of TAQ, electron conduction is still the bottleneck for further improving the rate performance of TAQ-based cathodes.

A cycling study of a TAQ-CB||Na cell at 200 mA g^{-1} (Figure 2h) reveals exceptional cycling stability with a capacity retention of 92% after 2000 cycles relative to the peak capacity. Interestingly, the discharge/charge voltage profiles undergo a clear transformation from a two-plateau curve to four plateaus within the first approximately 200 cycles. The profile then remains essentially unchanged throughout the next 1800 cycles (Figure 2h insets, Figure S23). This evolution indicates a gradual change of the charge storage mechanism to four single-electron processes. Upon even more prolonged cycling, the TAQ-CB||HC full cell delivers an electrode-level cathode capacity of 187 mAh $g^{-1}_{electrode}$ and an energy density of 336 Wh $kg^{-1}_{electrode}$ after 5000 cycles (ca. 2700 hours of cycling) at 800 mA g^{-1}, corresponding to a decline of only 7.4% relative to the peak capacity. This slow capacity decay (0.00148% per cycle) indicates a projected lifespan of ~13,500 cycles until the capacity retention drops to 80%. We note that although the presodiation of anodes may prove challenging to scale in practical SIBs, this treatment significantly enhances the ICE of full cells, effectively reduces the irreversible capacity loss, and improves the cycling stability, thereby demonstrating its important role in the potential commercialization of SIBs.[33-34] Additionally, using presodiated anodes also solves the sodium deficiency problem of most OEMs.

Figure 2i compares the more practically-relevant electrode-level energy density of TAQ with state-of-the-art OEMs. Although very few OEMs exhibit energy densities close to 1000 Wh kg^{-1} at the active-material level[35-36], which is far beyond that of inorganic cathode materials, an energy density of 500 Wh $kg^{-1}_{electrode}$ at the electrode level has never been achieved even at ultra-low current density of 10 mA g^{-1} due to the low active-material content (≤ 70 wt.%). Increasing the active-material content in the electrode formulation normally leads to drastic drop in performance. On the contrary, TAQ-CB cathodes are capable of delivering electrode-level energy densities of 501.5 Wh $kg^{-1}_{electrode}$ at 200 mA g^{-1} and 606 Wh $kg^{-1}_{electrode}$ at 25 mA g^{-1} (Source Data), which are higher than all organic and most of inorganic cathode materials for SIBs. Such enhanced performance is attributed to TAQ's high theoretical capacity, inherent insolubility, and its low

bandgap coupled with high electrical conductivity. TAQ-CB electrodes also reach a volumetric energy density of 723 Wh $L^{-1}_{electrode}$ based on the crystal-level density of approximately 2 g cm^{-3} and the electrode compact density of 1.1 g cm^{-3}, which is comparable to typical volumetric energy densities of Prussian blue analogue and polyanionic cathodes.[3-4]

Structural and morphological evolution of TAQ during charge storage

To understand the structural origin of the intrinsic high rate capability of TAQ, we conducted *in-operando* powder X-ray diffraction (PXRD) measurements to understand the structural changes of TAQ during Na^+ intercalation and deintercalation. Upon discharging at 0.1 A g^{-1} during the first cycle, the main reflection peak at 3.14 Å, which translates to the interlayer distance of pristine TAQ, gradually disappears, while a new peak at 3.23 Å starts growing after the intercalation of approximately 0.4 Na^+ per TAQ molecule (Figure 3a, pattern (a)), suggesting the formation of an intermediate phase. Further intercalation of Na^+ completely shifts the peak to 3.47 Å as Na_2TAQ forms at the end of the first discharge plateau (~1.8 V; Figure 3a, pattern (c)), via the intermediacy of another phase with an interlayer spacing of 3.34 Å (Figure 3a, pattern (b)). DFT calculations also confirm that Na^+ locates in-between molecular layers in Na_2TAQ (Figure 3b). Na_2TAQ continues to accommodate Na^+, converting to $Na_{3.5}$TAQ without major structural changes. Calculated crystal structures reveal interlayer distances of 3.42 Å for $Na_{2.5}$TAQ and 3.44 Å for $Na_{3.5}$TAQ, in good alignment with the experimental results. Surprisingly, further discharging towards Na_4TAQ induces significant structural disorder (Figure 3a, white circle, pattern (d)), which is likely due to the large crystal strain caused by deep intercalation of Na^+ and substantial electrostatic repulsion between TAQ^{4-}. Interestingly, DFT computed crystal structures reveal a drastic change of molecular packing from the layered stacking in $Na_{3.5}$TAQ to the offset stacking arrangement in Na_4TAQ (Figure 3b, S24), leading to a significantly increased face-to-face distance between TAQ^{4-} of 3.74 Å with a volume expansion larger than 20% compared to pristine TAQ. Therefore, we hypothesize that the formation of an almost amorphous Na_4TAQ phase upon the intercalation of the final 0.5 equivalent of Na^+ prevents the calculated substantial alteration of the layered structure, leading to significantly less volume expansion, which is crucial to promote rate and cycling performance (Figure 3e). Importantly, the structural transformations in the molecular TAQ lattices are reversible: crystalline Na_2TAQ phase emerges again upon re-charging (i.e., Na^+ deintercalation) through the first voltage plateau. Na_2TAQ further transforms into the recharged state (Figure 3a, pattern (e)), as the interlayer distance smoothly decreases from 3.47 Å to 3.23 Å. The recharged state corresponds approximately to $Na_{0.3}$TAQ based on the ICE of ~93%, and is independent of current density (Figure S25). This minimally sodiated state may be preferred thermodynamically: the few remaining Na^+ ions may play a structural role by providing a slightly open interlayer distance and thus facilitating Na^+ intercalation and diffusion, evidenced by the smooth variation of interlayer distance between 3.23 Å and 3.47 Å and ~30% less volume change in subsequent cycles.

In-operando PXRD measurements monitoring multiple Na^+ intercalation/deintercalation cycles at 0.2 A g^{-1} (Figure S25) further confirmed that the variation of the interlayer distance between 3.23 Å and 3.47 Å during cycling is highly reversible and stable. However, the disordered phase was almost invisible when the cell was discharged to 1.1 V because the capacity obtained at 0.2 A g^{-1}, 293 mAh g^{-1}, is lower than the value at 0.1 A g^{-1}, 316 mAh g^{-1}, and thus the intercalated Na^+ is not enough to induce the crystalline-to-disordered transition. The ability of TAQ to exhibit less structural alteration under higher current densities promotes its high rate capability. Remarkably, *in-operando* synchrotron wide-angle X-ray scattering measurements of a cell cycling at 1 A g^{-1} (Figure S26) reveal that the expansion of interlayer spacing to 3.47 Å is still facile under

high rate operation, indicating that the diffusion of Na^+ in the 2D pathways between layers is rapid and pose no limitation to the rate performance of TAQ. As a result, the maximal change in interlayer distance of TAQ is only 7.4% during the steady-state cycling (Figure 3e), suggesting that the Na^+ storage in TAQ is accompanied by only a small degree of volume expansion, again in line with computational results.

Based on the experimental and computational data above, we propose that the origin of TAQ's high rate capability is three-fold: 1) the in-plane hydrogen bonding network of TAQ provides structural integrity during Na^+ intercalation and deintercalation; 2) the vdW layered structure provides low-barrier 2D Na^+ diffusion pathways; 3) the favorable electronic structure of TAQ enables fast charge transport and transfer kinetics. Indeed, the microscopic morphology of TAQ crystallites remained almost unchanged upon discharging and recharging (Figure 3c), and no particle pulverization was observed even after long cycling (Figure 3d). The subtle exfoliation along the cross-section of the TAQ crystallites and the roughening of the crystallite surface likely further improve the rate performance of TAQ cathodes.[37] Furthermore, *ex-situ* DRUV-Vis-NIR spectra of TAQ cathodes at different states of discharge/charge confirm that their bandgaps are all equal to or below 0.6 eV (Figure 3e, S27), significantly lower than the pristine state.

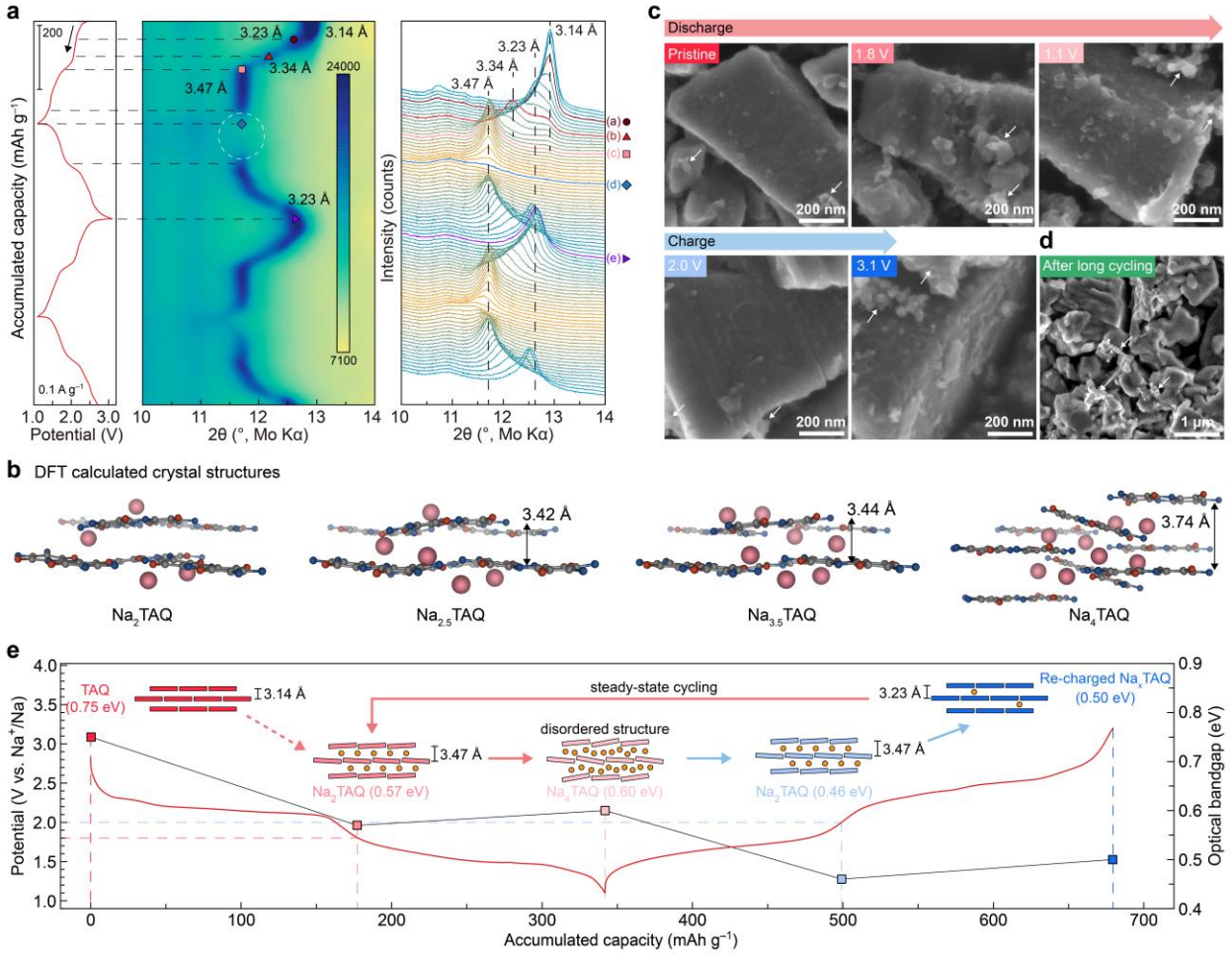

Figure 3. Structural changes of TAQ during discharge/charge. a, In-operando PXRD patterns of a TAQ||Na cell cycled at a current density of 100 mA g^{-1}. The voltage profile is shown on the left, and the individual PXRD patterns are shown on the right. **b,** DFT-computed crystal structures of Na_2TAQ, $Na_{2.5}$TAQ, $Na_{3.5}$TAQ, and Na_4TAQ. **c,** *Ex-situ* SEM images of TAQ cathodes at

different states of discharge/charge. **d,** An SEM image of a TAQ cathode after long cycling. White arrows in **c** and **d** indicate carbon black particles and binder. **e,** The first-cycle discharge/charge voltage profile of a representative TAQ-CB||Na cell at 25 mA g^{-1} with schematics of charge storage mechanism for TAQ. The re-charged state has an estimated formula of Na_xTAQ, where x is between 0.1 and 0.3 calculated from the ICE values. Square symbols indicate the optical bandgap of TAQ cathodes at different states of discharge/charge.

In-situ Growth of TAQ-CNT composites

With evidence at hand that the rate performance of TAQ cells may actually be gated by charge transport and *not* Na^+ diffusion, we sought to enhance the electrical conductivity of TAQ-based cathodes. Specifically, we focused on preparing composites of TAQ with carboxyl functionalized single-walled carbon nanotubes (cSWCNT). We denote these composites as TAQ-CNT*x*, where *x* represents *x* wt.% cSWCNTs in the composite. In contrast to previous strategies that rely on π–π interactions and normally require at least 20 wt.% CNTs,[10] TAQ-CNT*x* composites contain as little as 2~4 wt.% cSWCNTs, which is achieved through the *in-situ* formation and growth of TAQ crystals wrapped with cSWCNTs (Figure S28). We hypothesize that the carboxyl groups on the surface of cSWCNTs facilitate the growth of TAQ-CNT composite through hydrogen-bonding interaction and/or covalent bonding (i.e., amide formation) with amino groups of tetraamino-*p*-benzoquione (TAQ's precursor).[38] The TAQ-CNT composites exhibit high crystallinity (Figure 4a), and consist of TAQ micro-crystals that are closely wrapped and interconnected by cSWCNTs (Figure 4b, S29). Transmission electron microscopy (TEM) images of TAQ-CNT composites further confirm that cSWCNTs attach firmly to the surface of TAQ crystallites, forming an intimate contact (Figure 4c, S30). In comparison, using non-functionalized SWCNTs yielded poorly crystalline heterogeneous composites comprising detached nanoparticles (Figure S31). This difference supports our hypothesis that the strong interaction between surface carboxyl groups and TAQ play a crucial role in the composite synthesis and integrity.

The Raman spectrum of TAQ-CNT composite (Figure S32) shows a red shift of the G band from 1597 cm^{-1} in the pristine cSWCNTs to 1587 cm^{-1} in the composite, indicating a strong electronic coupling between TAQ and cSWCNTs. This doping-like interaction markedly enhances the electronic absorption of the composite below the optical bandgap of pristine TAQ (Figure 4d) and leads to a smaller bandgap of approximately 0.5 eV (Figure S33), which favorably impacts electron conduction and charge transfer. The TAQ-CNT composites demonstrate a notable enhancement in electrical conductivity, reaching 8.1 mS cm^{-1} for TAQ-CNT4 (Figure 4e), an approximately 400-fold increase over neat TAQ. To mimic the actual electrode formulation, we grinded TAQ or TAQ-CNT composites with CB to reach a total carbon content of 5 wt.% and compared their electrical conductivity (Figure S34). Both TAQ-CNT4/CB and TAQ-CNT2/CB mixtures are more conductive than the TAQ/CB mixture, with TAQ-CNT2/CB exhibiting the highest conductivity of 41.4 mS cm^{-1}.

Rate and cycling performance of TAQ-CNT cathodes

TAQ-CNT electrodes contain 90 wt.% TAQ, identical to TAQ-CB electrodes. They exhibit compact and crack-free coatings even under high mass loadings (> 10 mg cm^{-2}), likely due to the enhanced mechanical robustness brought by cSWCNTs (Figure S35). The TAQ-CNT4||Na cell exhibits a voltage profile very similar to a TAQ-CB||Na cell at 25 mA g^{-1} (Figure S36), but delivers an ICE of 100% and a lower overpotential of 0.23 V compared to 0.31 V for the TAQ-CB||Na cell.

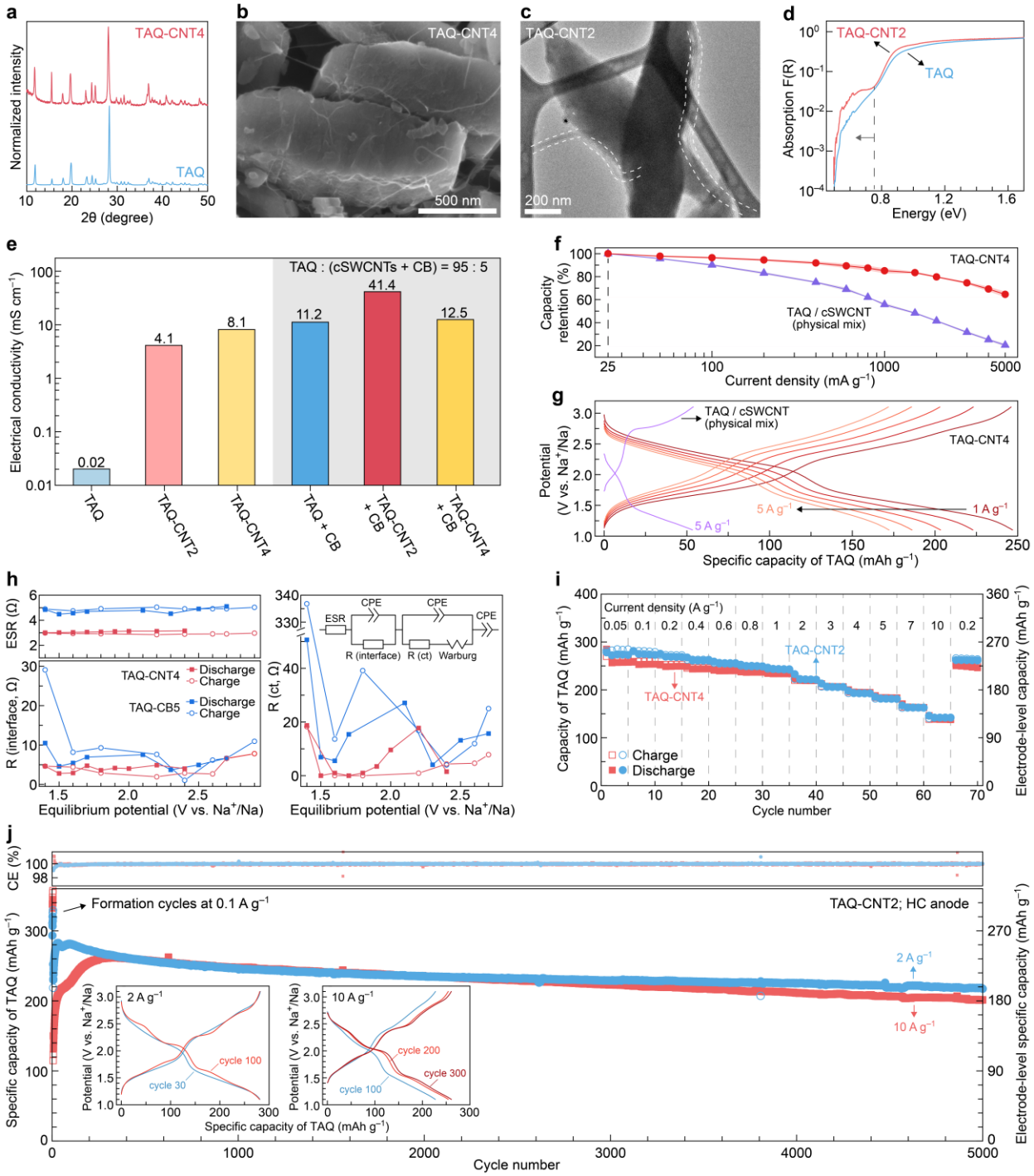

Figure 4. Characterization and battery performance of TAQ-cSWCNT composites. a, PXRD patterns of TAQ and TAQ-CNT4 composite. **b,** An SEM image of TAQ-CNT4 composite. **c,** A TEM image of TAQ-CNT2 composite. White dashed contours highlight cSWCNTs that wrap and interconnect TAQ crystals. **d,** Diffuse reflectance UV-Vis-NIR spectrum of TAQ-CNT2 composite, exhibiting enhanced electronic absorption below 0.75 eV (gray dashed line). **e,** Electrical conductivities of TAQ, TAQ-CNT composites, and their mixtures with CB. **f,** Comparison of CR_{25}^{m} ($50 \leq m \leq 5000$) for TAQ-CNT4 cathode and physically mixed TAQ/cSWCNT-based cathode. Both composites have the same amount of cSWCNTs. Color shaded areas indicate error bars based on two parallel cells. **g,** Discharge/charge voltage profiles

of the two cells in **f**. **h,** ESR, $R_{interface}$, and R_{ct} of TAQ-CB5 and TAQ-CNT4 based half cells at various equilibrium voltages during discharge and charge obtained by EIS studies. **i,** Rate capability studies of TAQ-CNT2||HC and TAQ-CNT4||HC full cells under current densities ranging from 0.05 A g^{-1} to 10 A g^{-1}. **j,** Cycling studies of TAQ-CNT2||HC full cells at 2 A g^{-1} and 10 A g^{-1}. Insets show selected voltage profiles during cycling.

TAQ-CNT cathodes exhibit a capacity retention CR_{25}^{1000} reaching 88.3% (Figure 4f), and deliver a capacity of 246 mAh g^{-1} at 1 A g^{-1}, which corresponds to an electrode-level capacity of 221 mAh $g^{-1}_{electrode}$, an improved power performance relative to both TAQ-CB5 and TAQ-CB20 cathodes. Moreover, TAQ-CNT cathodes deliver 167 mAh $g^{-1}_{electrode}$ at 5 A g^{-1} with a CR_{25}^{5000} value of 67.0%. This rate capability is superior compared to a control, physically mixed TAQ/cSWCNT composite, which exhibits 48 mAh $g^{-1}_{electrode}$ at 5 A g^{-1} with a CR_{25}^{5000} value of only 20.4% (Figure 4f, S37). TAQ-CNT cathodes also exhibit essentially unchanged cell polarization of approximately 0.24 V when the current density is raised from 25 mA g^{-1} to 1 A g^{-1} (Figure 4g). The resulting round-trip efficiency (RTE) is around 90%, a value commonly observed for commercial lithium-ion batteries. Although the polarization increases to 0.396 V at 5 A g^{-1} and the RTE decreases slightly to 83%, such performance is substantially better than that of physically mixed TAQ/cSWCNT composites, which exhibit a severe polarization of 1.425 V at 5 A g^{-1} with a RTE of 49%.

To reveal the origin of improved rate performance of TAQ-CNT composites, we employed GITT and determined that D_{Na^+} in the TAQ-CNT cathode is only marginally higher than in TAQ-CB cathodes (Figure S38). This confirmed that Na^+ diffusion does not limit the rate capability in TAQ-based electrodes. In contrast, EIS studies of TAQ-CNT4||Na cells at various states of discharge and charge (Figure 4h) reveal that the equivalent series resistances (ESR) decrease by more than 60% relative to TAQ-CB||Na cells, as expected due to the higher conductivity of TAQ-CNT4 composites. Thus, the intimate contact between TAQ crystals and cSWCNTs significantly enhances the interfacial charge transport kinetics, leading to lower overall interfacial resistances ($R_{interface}$). Moreover, the charge transfer resistances (R_{ct}) of TAQ-CNT4||Na cells are also lower than TAQ-CB||Na cells, indicating that cSWCNTs facilitate electron transfer kinetics of TAQ, likely through electronic coupling.

TAQ-CNT4||HC full cells exhibit better power performance than half cells, exhibiting a CR_{50}^{10000} of 53.4%. Interestingly, TAQ-CNT2 cathodes exhibit higher capacity than TAQ-CNT4 cathodes at current densities from 0.1 A g^{-1} to 10 A g^{-1} (Figure 4i). Notably, a respectable electrode-level capacity of 132 mAh $g^{-1}_{electrode}$ is recorded for a TAQ-CNT2 electrode at a current density as high as 10 A g^{-1}, corresponding to a charging time of less than one minute. The same cell recovers to a capacity of 266 mAh g^{-1} when the current density is reduced from 10 A g^{-1} to 0.2 A g^{-1}, a negligible drop from the initial capacity of 269 mAh g^{-1} at 0.2 A g^{-1} (Figure 4i). Stable repeated switching between ~300 mAh g^{-1} at 0.1 A g^{-1} and ~130 mAh g^{-1} at 10 A g^{-1} further showcases the ability of TAQ-CNT2 cathodes to tolerate abrupt power fluctuations and fulfill peak power requirements for most energy storage systems (Figure S39).

Cycling of a TAQ-CNT2||HC full cell at 2 A g^{-1} reveals an electrode-level cathode capacity of 196 mAh $g^{-1}_{electrode}$ after 5000 cycles, corresponding to a capacity retention of 94% relative to the initial capacity after formation cycles (Figure 4j). Remarkably, increasing the current density to 10 A g^{-1} showed almost no decrease of the peak capacity, meanwhile delivering an electrode-level cathode capacity of 181.2 mAh $g^{-1}_{electrode}$ after 5000 cycles. Importantly, TAQ-CNT2||HC full cells

exhibit stabilized average discharge voltages of 1.97 V at 2 A g^{-1} and 1.94 V at 10 A g^{-1} (Figure S40), which are essentially unchanged relative to the value obtained at 25 mA g^{-1}. Although the average polarization of cells increases to 0.447 V at 10 A g^{-1}, the average RTE only drops slightly to 80%. An attempt to cycle a TAQ-CNT2||HC full cell at an ultrahigh current density of 20 A g^{-1} reveals a peak electrode-level discharge capacity of 135 mAh $g^{-1}_{electrode}$ after charging for less than 30 seconds (Figure S41). Although the power performance is limited by the rate capability of the anode, this cell still delivers electrode-level energy and power densities of 241 Wh $kg^{-1}_{electrode}$ and 31.6 kW $kg^{-1}_{electrode}$, respectively.

Effects of mass loadings on full-cell performance

Increasing the areal mass loading of OEMs to approach practical levels commonly leads to a drastic drop of their electrochemical performance. Consequently, organic cathodes for SIBs are generally tested at low mass loadings, commonly 1-2 mg cm^{-2}, which translate to inferior areal capacities. Figure 5 shows that TAQ-CNT electrodes exhibit almost loading-independent performance, as indicated by the linear relationship between areal mass loadings and areal capacities, whereas the areal capacities of other organic cathodes usually plateau out with increasing mass loadings due to poor electron and/or ion transport. Notably, a practical level areal capacity of 4.5 mAh cm^{-2} is achieved in a TAQ-CNT||HC full cell with 16.2 mg cm^{-2} of TAQ and an N/P ratio of 1.2 (Figure S42), outperforming most organic cathodes. This cell also delivers a specific energy density of 182 Wh kg^{-1} based on the total mass of both cathode and anode, including conductive carbon and binder. This is superior to the most promising organic batteries with much lower mass loadings and is comparable with state-of-the-art inorganic full cells (Figure S43 and Table S3). Although the rate capability slightly reduces with increasing mass loading, 2.3 mAh cm^{-2} can still be achieved under a high areal current density of 3.2 mA cm^{-2}, suggesting promising power performance at the practical level. We expect that electrode-level engineering, such as the optimization of cathode porosity and electrode architecture for better ion and charge transport, and cell-level engineering, such as using high-capacity anodes (e.g., phosphorus and tin),[39] would further improve the energy and power performance of TAQ-based SIBs even at high mass loadings.[40-41]

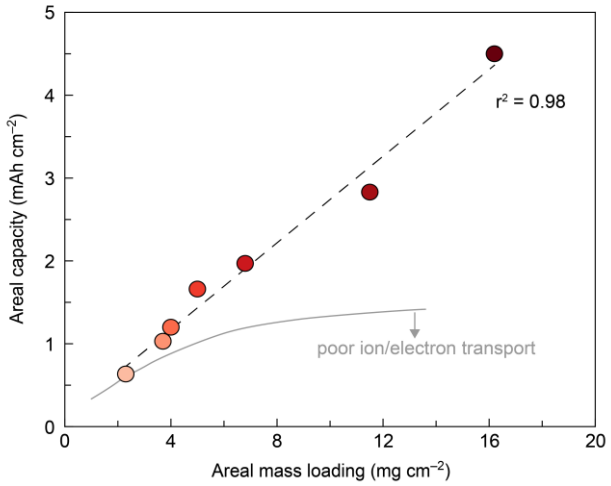

Figure 5. Effects of mass loading on electrode performance of TAQ-based cathodes. Dependence of areal capacity on TAQ mass loading of TAQ-CNT cathodes. The black dash line indicates the best linear fit. The gray line represents a typical dependence curve when ion and/or electron transport in electrodes are not good.

Benchmarking TAQ-based cathodes against other cathode material classes for SIBs

Organic cathodes for SIBs commonly exhibit less practically competitive electrode-level gravimetric specific energies (≤ 400 Wh $kg^{-1}_{electrode}$) compared to their inorganic counterparts, which can exhibit specific energies exceeding 600 Wh $kg^{-1}_{electrode}$ (Figure 2g, 6a, S44, S45). Although a few OEMs exhibit specific energies between 400 Wh $kg^{-1}_{electrode}$ and 500 Wh $kg^{-1}_{electrode}$, they either involve anion insertion[42], or have an average discharge voltage that is not ideal as a cathode (i.e., ≤ 1.5 V)[36]. They further often suffer from poor cycling stability due to severe dissolution[43]. Additionally, organic cathodes normally exhibit good rate capability only when considerable amount of conducting additives are used, so their electrode-level energy densities under high rates (e.g., ≥ 2 A g^{-1}) are still less satisfactory than those of inorganic cathodes. In contrast, TAQ-based cathodes show competitive electrode-level energy densities compared to state-of-the-art O3-type layered transition-metal oxides at low rates, and deliver ~30% or even greater than 100% more energy than inorganic cathodes at approximately 2 A g^{-1} and 10 A g^{-1}, respectively (Figure 6a). More relevantly, TAQ-based cathodes exhibit better power and energy performance compared to inorganic cathodes under the same charging/discharging time, while evidently significantly outperforming other organic cathodes. Specifically, TAQ-CNT cathodes exhibit a power density of 18 kW $kg^{-1}_{electrode}$ at 10 A g^{-1}, which is comparable to state-of-the-art capacitive and pseudocapacitive materials (Figure 6b), while delivering 2~6-fold higher energy density reaching 472 Wh $kg^{-1}_{electrode}$.

Cycling stability is another important performance metric for batteries, especially for practical applications. We employ both capacity loss per cycle and total cycle time to thoroughly evaluate the cycling stability of organic and inorganic SIB cathodes. TAQ-based cathodes exhibit one of the lowest capacity loss per cycle, corresponding to projected cycle numbers far exceeding 5000 before the capacity drops to 80%. The reported cycle time of most inorganic and organic cathodes under more practical current densities (i.e., > 0.1 A g^{-1}) is lower than 1800 hours due to various reasons, such as chemical/structural instability and dissolution. TAQ-based cathodes can continuously cycle for more than 1800 hours under a large range of current densities (Figure 6c).

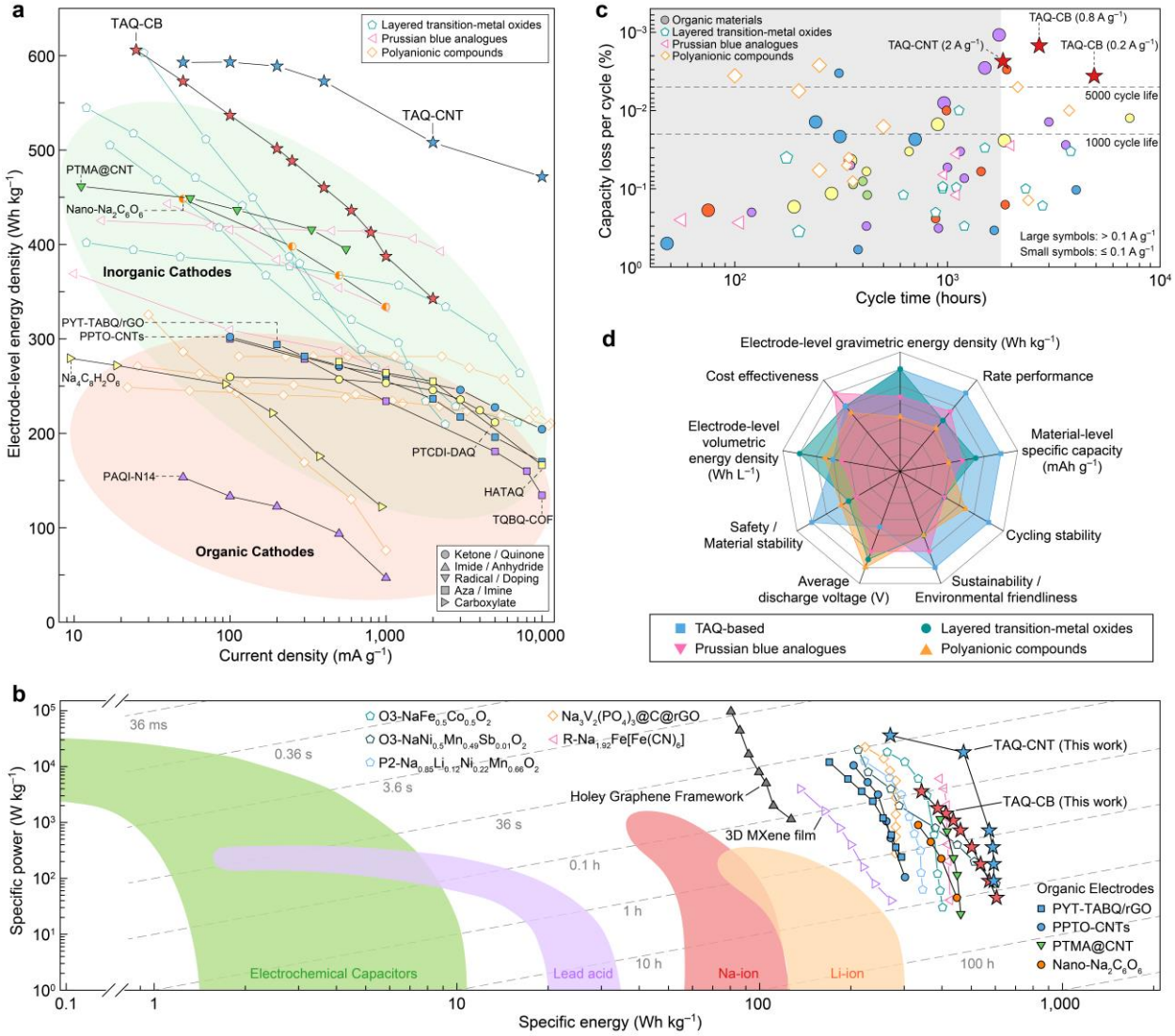

Figure 6. Benchmarking TAQ-based cathodes against state-of-the-art organic and inorganic SIB cathodes. a, A comparison of the electrode-level gravimetric energy densities of TAQ-based cathodes with the best organic and inorganic cathodes at current densities ranging from 10 mA g^{-1} to 10,000 mA g^{-1}. Colors of scatters represent different strategies: yellow (immobilization by large amount of carbon); green (involving anionic redox); blue (employing advanced carbon materials); purple (polymerization/framework formation); orange (salinization). Half-hollow scatters indicate average discharge voltage less than or equal to 1.5 V. A complete comparison and the list of examples can be found in Figure S44, S45. **b,** Ragone plot of TAQ-based cathodes and selected inorganic and organic cathodes. State-of-the-art capacitive (Holey Graphene Framework) and pseudocapacitive (3D porous MXene film) materials are also presented for comparison. Colored areas represent performance metrics of commercial devices. **c,** Capacity loss per cycle against cycle time of TAQ, organic, and inorganic cathode materials. The shadow area indicates cycle time of less than 1800 hours. Same color codes for organic electrodes were applied as in **a**. **d,** SIB cathode performance assessments of TAQ, layered transition-metal oxides, Prussian blue analogues, and polyanionic compounds.

Discussion

Although organic cathodes generally show lower average discharge voltage compared to inorganic cathodes, TAQ-based cathodes and full cells exhibit highly competitive energy densities relative to commercially promising inorganic cathode technologies due to the high electrode-level specific capacity of TAQ-based electrodes (Figure 6d). TAQ-based SIBs also outperform $LiFePO_4$-based lithium-ion batteries in both energy and power densities. In practical applications such as electric vehicles (EVs), although a lower cell voltage leads to a higher number of cells in series to fulfill certain voltage requirements, TAQ-based cells have low impedance due to the satisfactory electron and ion transport properties of TAQ, circumventing the Joule heating issue. Therefore, TAQ-based SIBs show great potential as a cost-effective replacement for $LiFePO_4$-based LIBs in moderate-range five-passenger EVs and in applications requiring the storage and release of regenerative braking energy.[44] Furthermore, TAQ exhibits excellent material stability against air and moisture, superior rate performance, long lifespan, environmental friendliness, and sustainability (Figure 6d), a series of "soft" metrics that provide it with practical competitiveness as a cathode material for SIBs serving large-scale stationary energy storage applications, especially where high-quality power regulation is required.

In conclusion, we have demonstrated that TAQ cathodes for SIBs exhibit both high energy and power densities at the electrode level due to the combination of TAQ's low electronic bandgap with fast electron transport, facile 2D Na^+ diffusion pathways, and insolubility in electrolytes. Wrapping and interconnecting TAQ crystals with CNTs further improves the electrical conductivity of the cathode composite, leading to ultrahigh rate capability. Our results demonstrate the competitiveness of organic cathodes for SIBs and provide blueprints for future development of organic SIBs.

Experimental procedures

Electrode fabrication and electrochemical tests

TAQ electrodes were tested in CR2032 coin cells assembled in an Ar-filled glove box. All electrodes were prepared under ambient conditions. TAQ composite electrodes contained 90 wt.% of TAQ, 5 wt.% of carbon black (CB), 4 wt.% of carboxymethyl cellulose (CMC), and 1 wt.% of styrene butadiene rubber (SBR). For TAQ-cSWCNT electrodes, CB and cSWCNT together contribute 5 wt.% of the cathode mass. CMC and SBR were well dissolved/suspended in a small amount of water (50~100 μL/mg) upon heating at 85 °C with vigorous stirring for an hour. Well-mixed TAQ (or TAQ-cSWCNT) and CB powders (upon grinding) were transferred into the CMC/SBR aqueous mixture, and the resulting mixture was vigorously stirred at 85 °C for an hour to produce the cathode slurry, which was then coated onto stainless steel disks. All electrodes were dried under ambient conditions before drying in a vacuum oven at 100 °C for 12 hours. TAQ undergoes in-situ morphological change through the fracture of micro-rods preferentially along the cross-section direction during electrode fabrication, turning into sub-micron rhombic plates. TAQ-based electrodes had TAQ loadings between 1.5 and 3.0 mg cm^{-2} for most of the tests. Higher mass loading studies used electrodes with TAQ loadings ranging between 4 mg cm^{-2} and 16 mg cm^{-2}. Half cells used a metallic Na pellet as the anode (thickness ~500 μm). Full cells used a Na pre-doped hard carbon (HC) coated on Al foil as the anode. Glass microfiber (Whatman GF/D) was used as the separator. To fabricate Na pre-doped HC electrodes, commercial HC anode on Al foil (92 wt.% of HC, MTI Corporation, 8 mg cm^{-2}, coating thickness ~90 μm, Al foil thickness 16 μm) was cut into 15-mm disks (~13 mg of HC per disk), and the resulting electrodes were sodiated electrochemically in HC||Na cells by constant current discharge at a current of 0.2

mA. Coin cells were typically tested between 1.1 V and 3.1 V versus Na^+/Na using Landt battery cyclers at room temperature (25 °C). Galvanostatic Intermittent Titration Technique (GITT), cyclic voltammetry, and EIS tests were performed using a BioLogic VMP-3 workstation. GITT measurements were carried out at a current density of 25 mA g^{-1}. Each step consisted of a one-hour constant-current discharge or charge followed by a two-hour rest. Symmetric cells were assembled using one fully discharged TAQ electrode and one pristine TAQ electrode, with both electrodes having identical active material loading. The cells were cycled at 25 mA g^{-1} for one cycle before the EIS measurements. Impedance data for coin cells was collected from 10 mHz to 1 MHz at various potentials.

In-operando powder X-ray diffraction

The in-operando PXRD measurements were performed using custom-made half-cells with a 10-μm-thick Al foil window on a Panalytical Empyrean diffractometer equipped with a Mo X-ray source, focusing mirror and Galipix 3D detector.[15] The corresponding electrodes were prepared as thin films by repeated kneading and rolling of a slurry of TAQ, carbon black, and polytetrafluoroethylene (PTFE) with a mass ratio of 6:3:1 in ethanol. The prepared films were dried at 100 ℃ for at least 12 hours and pressed onto stainless steel mesh prior to use. To enhance the intensities of PXRD signals, TAQ mass loading of between 8 mg cm^{-2} and 10 mg cm^{-2} was used. The PXRD patterns were recorded in the Bragg-Brentano θ/2θ geometry using an in-operando coin cell battery holder. The in-operando half cells used metallic Na pellets as the anode. The coin cells were cycled under constant current between 1.1 V and 3.1 V while PXRD patterns were recorded.

Data availability

All data are available in the main text and supplementary information.

References

1. Tarascon, J.-M., Na-ion versus Li-ion Batteries: Complementarity Rather than Competitiveness. *Joule* **2020,** *4* (8), 1616-1620.
2. Zuo, W.; Innocenti, A.; Zarrabeitia, M.; Bresser, D.; Yang, Y.; Passerini, S., Layered Oxide Cathodes for Sodium-Ion Batteries: Storage Mechanism, Electrochemistry, and Techno-economics. *Accounts of Chemical Research* **2023,** *56* (3), 284-296.
3. Peng, J.; Zhang, W.; Liu, Q.; Wang, J.; Chou, S.; Liu, H.; Dou, S., Prussian Blue Analogues for Sodium-Ion Batteries: Past, Present, and Future. *Advanced Materials* **2022,** *34* (15), 2108384.
4. Xu, C.; Zhao, J.; Yang, C.; Hu, Y.-S., Polyanionic Cathode Materials for Practical Na-Ion Batteries toward High Energy Density and Long Cycle Life. *ACS Central Science* **2023,** *9* (9), 1721-1736.
5. Xu, S.; Dong, H.; Yang, D.; Wu, C.; Yao, Y.; Rui, X.; Chou, S.; Yu, Y., Promising Cathode Materials for Sodium-Ion Batteries from Lab to Application. *ACS Central Science* **2023,** *9* (11), 2012-2035.
6. Zhang, H.; Gao, Y.; Liu, X. H.; Yang, Z.; He, X. X.; Li, L.; Qiao, Y.; Chen, W. H.; Zeng, R. H.; Wang, Y.; Chou, S. L., Organic Cathode Materials for Sodium-Ion Batteries: From Fundamental Research to Potential Commercial Application. *Advanced Functional Materials* **2021,** *32* (4).
7. Poizot, P.; Gaubicher, J.; Renault, S.; Dubois, L.; Liang, Y.; Yao, Y., Opportunities and Challenges for Organic Electrodes in Electrochemical Energy Storage. *Chem Rev* **2020**.
8. Augustyn, V.; Come, J.; Lowe, M. A.; Kim, J. W.; Taberna, P. L.; Tolbert, S. H.; Abruna, H. D.; Simon, P.; Dunn, B., High-rate electrochemical energy storage through Li+ intercalation pseudocapacitance. *Nat Mater* **2013,** *12* (6), 518-22.
9. Song, Z.; Qian, Y.; Zhang, T.; Otani, M.; Zhou, H., Poly(benzoquinonyl sulfide) as a High-Energy Organic Cathode for Rechargeable Li and Na Batteries. *Adv Sci (Weinh)* **2015,** *2* (9), 1500124.

10. Shi, R.; Liu, L.; Lu, Y.; Li, Y.; Zheng, S.; Yan, Z.; Zhang, K.; Chen, J., In Situ Polymerized Conjugated Poly(pyrene-4,5,9,10-tetraone)/Carbon Nanotubes Composites for High-Performance Cathode of Sodium Batteries. *Advanced Energy Materials* **2020,** *11* (6).
11. Shi, R.; Liu, L.; Lu, Y.; Wang, C.; Li, Y.; Li, L.; Yan, Z.; Chen, J., Nitrogen-rich covalent organic frameworks with multiple carbonyls for high-performance sodium batteries. *Nat Commun* **2020,** *11* (1), 178.
12. Wang, J.; Liu, X.; Jia, H.; Apostol, P.; Guo, X.; Lucaccioni, F.; Zhang, X.; Zhu, Q.; Morari, C.; Gohy, J.-F.; Vlad, A., A High-Voltage Organic Framework for High-Performance Na- and K-Ion Batteries. *ACS Energy Letters* **2022**, 668-674.
13. Wang, S.; Wang, L.; Zhu, Z.; Hu, Z.; Zhao, Q.; Chen, J., All organic sodium-ion batteries with Na(4)C(8)H(2)O(6). *Angew Chem Int Ed Engl* **2014,** *53* (23), 5892-6.
14. Chen, T.; Banda, H.; Yang, L.; Li, J.; Zhang, Y.; Parenti, R.; Dincă, M., High-rate, high-capacity electrochemical energy storage in hydrogen-bonded fused aromatics. *Joule* **2023,** *7* (5), 986-1002.
15. Chen, T.; Banda, H.; Wang, J.; Oppenheim, J. J.; Franceschi, A.; Dincă, M., A Layered Organic Cathode for High-Energy, Fast-Charging, and Long-Lasting Li-Ion Batteries. *ACS Central Science* **2024,** *10* (3), 569-578.
16. Li, Z.; Jia, Q.; Chen, Y.; Fan, K.; Zhang, C.; Zhang, G.; Xu, M.; Mao, M.; Ma, J.; Hu, W.; Wang, C., A Small Molecular Symmetric All-Organic Lithium-Ion Battery. *Angew Chem Int Ed Engl* **2022,** *61* (33), e202207221.
17. Yin, X.; Sarkar, S.; Shi, S.; Huang, Q. A.; Zhao, H.; Yan, L.; Zhao, Y.; Zhang, J., Recent Progress in Advanced Organic Electrode Materials for Sodium-Ion Batteries: Synthesis, Mechanisms, Challenges and Perspectives. *Advanced Functional Materials* **2020,** *30* (11).
18. Novikova, S. A.; Larkovich, R. V.; Chekannikov, A. A.; Kulova, T. L.; Skundin, A. M.; Yaroslavtsev, A. B., Electrical Conductivity and Electrochemical Characteristics of Na3V2(PO4)3-Based NASICON-Type Materials. *Inorganic Materials* **2018,** *54* (8), 794-804.
19. Westman, K.; Dugas, R.; Jankowski, P.; Wieczorek, W.; Gachot, G.; Morcrette, M.; Irisarri, E.; Ponrouch, A.; Palacín, M. R.; Tarascon, J. M.; Johansson, P., Diglyme Based Electrolytes for Sodium-Ion Batteries. *ACS Applied Energy Materials* **2018,** *1* (6), 2671-2680.
20. Tian, Z.; Zou, Y.; Liu, G.; Wang, Y.; Yin, J.; Ming, J.; Alshareef, H. N., Electrolyte Solvation Structure Design for Sodium Ion Batteries. *Advanced Science* **2022,** *9* (22), 2201207.
21. Li, Y.; Wu, F.; Li, Y.; Liu, M.; Feng, X.; Bai, Y.; Wu, C., Ether-based electrolytes for sodium ion batteries. *Chem Soc Rev* **2022,** *51* (11), 4484-4536.
22. Sieuw, L.; Jouhara, A.; Quarez, E.; Auger, C.; Gohy, J. F.; Poizot, P.; Vlad, A., A H-bond stabilized quinone electrode material for Li-organic batteries: the strength of weak bonds. *Chem Sci* **2019,** *10* (2), 418-426.
23. Jouhara, A.; Dupré, N.; Gaillot, A.-C.; Guyomard, D.; Dolhem, F.; Poizot, P., Raising the redox potential in carboxyphenolate-based positive organic materials via cation substitution. *Nature Communications* **2018,** *9* (1), 4401.
24. Xiong, W.; Huang, W.; Zhang, M.; Hu, P.; Cui, H.; Zhang, Q., Pillar[5]quinone–Carbon Nanocomposites as High-Capacity Cathodes for Sodium-Ion Batteries. *Chemistry of Materials* **2019,** *31* (19), 8069-8075.
25. Luo, W.; Allen, M.; Raju, V.; Ji, X., An Organic Pigment as a High-Performance Cathode for Sodium-Ion Batteries. *Advanced Energy Materials* **2014,** *4* (15).
26. Song, J.; Park, S.; Kim, S.; Mathew, V.; Alfaruqi, M. H.; Jo, J.; Kim, J., Uniform Carbon Coated Na3V2(PO4)2O2xF3–2x Nanoparticles for Sodium Ion Batteries as Cathode. *ACS Sustainable Chemistry & Engineering* **2019,** *7* (23), 18826-18834.
27. Palanisamy, K.; Daboss, S.; Romer, J.; Schäfer, D.; Rohnke, M.; Flowers, J. K.; Fuchs, S.; Stein, H. S.; Fichtner, M.; Kranz, C., Microscopic and Spectroscopic Analysis of the Solid Electrolyte Interphase at Hard Carbon Composite Anodes in 1 M NaPF6/Diglyme. *Batteries & Supercaps* **2024,** *7* (3), e202300482.

28. Kim, T.; Choi, W.; Shin, H.-C.; Choi, J.-Y.; Kim, J. M.; Park, M.-S.; Yoon, W.-S., Applications of Voltammetry in Lithium Ion Battery Research. *Journal of Electrochemical Science and Technology* **2020,** *11* (1), 14-25.
29. Wang, Q.; Jiang, K.; Feng, Y.; Chu, S.; Zhang, X.; Wang, P.; Guo, S.; Zhou, H., P2-Type Layered Na(0.75)Ni(1/3)Ru(1/6)Mn(1/2)O(2) Cathode Material with Excellent Rate Performance for Sodium-Ion Batteries. *ACS Appl Mater Interfaces* **2020,** *12* (35), 39056-39062.
30. Momma, T.; Yokoshima, T.; Nara, H.; Gima, Y.; Osaka, T., Distinction of impedance responses of Li-ion batteries for individual electrodes using symmetric cells. *Electrochimica Acta* **2014,** *131*, 195-201.
31. Ogihara, N.; Itou, Y.; Sasaki, T.; Takeuchi, Y., Impedance Spectroscopy Characterization of Porous Electrodes under Different Electrode Thickness Using a Symmetric Cell for High-Performance Lithium-Ion Batteries. *The Journal of Physical Chemistry C* **2015,** *119* (9), 4612-4619.
32. Yoon, S.-B.; Jegal, J.-P.; Roh, K. C.; Kim, K.-B., Electrochemical Impedance Spectroscopic Investigation of Sodium Ion Diffusion in MnO2 Using a Constant Phase Element Active in Desired Frequency Ranges. *Journal of The Electrochemical Society* **2014,** *161* (4), H207.
33. Mu, J.-J.; Liu, Z.-M.; Lai, Q.-S.; Wang, D.; Gao, X.-W.; Yang, D.-R.; Chen, H.; Luo, W.-B., An industrial pathway to emerging presodiation strategies for increasing the reversible ions in sodium-ion batteries and capacitors. *Energy Materials* **2022,** *2* (6).
34. Zhang, M.; Li, Y.; Wu, F.; Bai, Y.; Wu, C., Boost sodium-ion batteries to commercialization: Strategies to enhance initial Coulombic efficiency of hard carbon anode. *Nano Energy* **2021,** *82*.
35. Kuan, H.-C.; Luu, N. T. H.; Ivanov, A. S.; Chen, T.-H.; Popovs, I.; Lee, J.-C.; Kaveevivitchai, W., A nitrogen- and carbonyl-rich conjugated small-molecule organic cathode for high-performance sodium-ion batteries. *Journal of Materials Chemistry A* **2022,** *10* (30), 16249-16257.
36. Lee, M.; Hong, J.; Lopez, J.; Sun, Y.; Feng, D.; Lim, K.; Chueh, W. C.; Toney, M. F.; Cui, Y.; Bao, Z., High-performance sodium–organic battery by realizing four-sodium storage in disodium rhodizonate. *Nature Energy* **2017,** *2* (11), 861-868.
37. Lukatskaya, M. R.; Mashtalir, O.; Ren, C. E.; Dall'Agnese, Y.; Rozier, P.; Taberna, P. L.; Naguib, M.; Simon, P.; Barsoum, M. W.; Gogotsi, Y., Cation Intercalation and High Volumetric Capacitance of Two-Dimensional Titanium Carbide. *Science* **2013,** *341* (6153), 1502-1505.
38. Acosta-Guzmán, P.; Ojeda-Porras, A.; Gamba-Sánchez, D., Contemporary Approaches for Amide Bond Formation. *Advanced Synthesis & Catalysis* **2023,** *365* (24), 4359-4391.
39. Chang, G.; Zhao, Y.; Dong, L.; Wilkinson, D. P.; Zhang, L.; Shao, Q.; Yan, W.; Sun, X.; Zhang, J., A review of phosphorus and phosphides as anode materials for advanced sodium-ion batteries. *Journal of Materials Chemistry A* **2020,** *8* (10), 4996-5048.
40. Sun, H.; Mei, L.; Liang, J.; Zhao, Z.; Lee, C.; Fei, H.; Ding, M.; Lau, J.; Li, M.; Wang, C.; Xu, X.; Hao, G.; Papandrea, B.; Shakir, I.; Dunn, B.; Huang, Y.; Duan, X., Three-dimensional holey-graphene/niobia composite architectures for ultrahigh-rate energy storage. *Science* **2017,** *356* (6338), 599-604.
41. Gallagher, K. G.; Trask, S. E.; Bauer, C.; Woehrle, T.; Lux, S. F.; Tschech, M.; Lamp, P.; Polzin, B. J.; Ha, S.; Long, B.; Wu, Q.; Lu, W.; Dees, D. W.; Jansen, A. N., Optimizing Areal Capacities through Understanding the Limitations of Lithium-Ion Electrodes. *Journal of The Electrochemical Society* **2016,** *163* (2), A138.
42. Gannett, C. N.; Peterson, B. M.; Melecio-Zambrano, L.; Trainor, C. Q.; Fors, B. P.; Abruña, H. D., Performance optimization and fast rate capabilities of novel polymer cathode materials through balanced electronic and ionic transport. *Journal of Materials Chemistry A* **2021,** *9* (9), 5657-5663.
43. Liu, X.; Ye, Z., Nitroaromatics as High-Energy Organic Cathode Materials for Rechargeable Alkali-Ion (Li+, Na+, and K+) Batteries. *Advanced Energy Materials* **2020,** *11* (4).
44. Rudola, A.; Sayers, R.; Wright, C. J.; Barker, J., Opportunities for moderate-range electric vehicles using sustainable sodium-ion batteries. *Nature Energy* **2023,** *8* (3), 215-218.

Acknowledgments: This work was supported by Automobili Lamborghini S.p.A. This work was carried out in part through the use of MIT.nano's facilities. Cryo-EM specimens were prepared and imaged at the Automated Cryogenic Electron Microscopy Facility in MIT.nano on a Talos Arctica microscope, a gift from the Arnold and Mabel Beckman Foundation. This research used the resources of the Center for Functional Nanomaterials (CFN), the SMI beamline (12-ID) of the National Synchrotron Light Source II, a U.S. Department of Energy (DOE) Office of Science User Facility operated for the DOE Office of Science by Brookhaven National Laboratory under Contract No. DE-SC0012704.

Author contributions: T.C. and J.W. contribute equally. Conceptualization: T.C., J.W., H.B., and M.D. Methodology: T.C., and J.W. Investigation: T.C., J.W., B.T., K.Z., H.B., Y.Z., and D.K. Visualization: T.C., and J.W. Writing – original draft: T.C., and J.W. Writing – review & editing: T.C., J.W., B.T., K.Z., H.B., Y.Z., D.K., and M.D. Supervision: M.D.

Competing interests: M.D., H.B., T.C., J.W., and B.T. have pending patent and/or provisional patent applications covering the technology described here. The remaining authors declare no competing interests.

Additional information

Supplementary information The online version contains available supplementary material.